



Technical note: Identification of two ice-nucleating regimes for dust-related cirrus clouds based on the relationship between number concentrations of ice-nucleating particles and ice crystals

Yun He^{1,2,3,*}, Zhenping Yin^{4,*}, Fuchao Liu^{1,2,3}, Fan Yi^{1,2,3}

¹School of Electronic Information, Wuhan University, Wuhan 430072, China

²Key Laboratory of Geospace Environment and Geodesy, Ministry of Education, Wuhan 430072, China

³State Observatory for Atmospheric Remote Sensing, Wuhan 430072, China.

⁴School of Remote Sensing and Information Engineering, Wuhan University, Wuhan 430072, China.

10 *Correspondence to:* Yun He (heyun@whu.edu.cn), Zhenping Yin (zp.yin@whu.edu.cn)

Abstract. Large amounts of dust aerosols are lifted to the upper troposphere every year and play a major role in cirrus formation by acting as efficient ice nuclei. However, the relative importance of heterogeneous nucleation and spontaneous homogenous nucleation in dust-related cirrus clouds is still not well evaluated globally. Here, based on space-borne observations, we propose a method to identify two ice-nucleating regimes of dust-related cirrus clouds, i.e., (1) sole presence of heterogeneous nucleation and (2) competition between heterogeneous and homogeneous nucleation, by characterizing the relationship between dust ice-nucleating particle concentrations (INPC) calculated from the Cloud-Aerosol Lidar with Orthogonal Polarization (CALIOP) using the POLarization LIdar PHOtometer Networking (POLIPHON) method and in-cloud ice crystal number concentration (ICNC) from the DARDAR (LiDAR/raDAR) dataset. Two typical cirrus cases over central China are shown as a demonstration. In the first case, the upper part (near the cloud top) of a series of cirrus clouds successfully realized the INPC-ICNC closure, meaning that heterogeneous nucleation solely takes place; while the lower part of cirrus clouds showed the possible competition between heterogeneous and homogeneous nucleation. In the second case, the ICNCs in cirrus cloud dramatically exceeded the dust INPCs in the vicinity by more than an order of magnitude, revealing that besides dust-induced heterogeneous nucleation, homogeneous nucleation also participated in ice formation and produced the additional ice crystals. The proposed identification method is anticipated to apply in evaluating the influence of upper-troposphere dust on global cirrus formation and investigating the potential positive role of cirrus cloud thinning in the offset of climate warming.

1 Introduction

Cirrus clouds, composed of pure ice crystals, widely exist at the high altitude of the troposphere from ~5 km to up to the tropopause, where the temperatures are usually below -38 °C (Heymsfield et al., 2017; Ge et al., 2018; Krämer et al., 2020). They approximately cover 20-25% of Earth's surface at any given time (Maloney et al., 2022), play a crucial role in climate



30 by altering the balance of solar and terrestrial radiation (IPCC, 2013), and potentially modulate water vapor balance between the upper troposphere and the lower stratosphere via convection (Jensen et al., 2013).

Cirrus clouds contribute a large uncertainty in general circulation model, resulting in an inadequate accuracy in predicting the rate and geographical pattern of climate change (Heymsfield et al., 2017). Due to the variety of their microphysical properties (particle size, number, and shape), it is even a challenge to convincingly draw a qualitative conclusion that cirrus clouds cause either warming or cooling effect (Wolf et al., 2019). Cirrus clouds are typically classified into two categories in terms of forming mechanisms: in situ-origin cirrus and liquid-origin cirrus (Krämer et al., 2016, 2020). In situ-origin cirrus forms at colder altitudes (< -38 °C) accompanying with either fast updraft or slow updraft. In fast updraft situation, homogeneous freezing is the dominated freezing type since ice supersaturation quickly increases up to the homogeneous freezing threshold; in slow updraft situation, heterogeneous freezing (deposition freezing) is dominant first because ice supersaturation lies between the heterogeneous and homogeneous freezing threshold (Krämer et al., 2009) and later homogeneous freezing is followed due to the depletion of ice-nucleating particles and the persistence of cooling. Liquid-origin cirrus completely forms through heterogeneous freezing (immersion and contact freezing) and then is uplifted to the colder altitudes. Recently, numerous studies have reported that many types of aerosols existing at the upper troposphere (cirrus altitudes) can serve as effective ice-nucleating particles (INPs) (Cziczo et al., 2013), such as aviation soot (Teschke et al., 2016; Righi et al., 2021), volcanic aerosols (Sporre et al., 2022), wildfire smoke (Ansmann et al., 2021; Hu et al., 2022), dust aerosols (Kuebbeler et al., 2014), and so on, making the in-situ heterogeneous formation at cirrus altitudes possible.

In consideration of the emission load and ice-nucleating efficiency, dust is the essential type among the upper-tropospheric INP particles. Abundant dust aerosols are elevated from the surface of desert areas by wind and convection every year and then are mainly transported in the lower and middle troposphere (He et al., 2015, 2021a; Yin et al., 2021; Guo et al., 2017). Occasionally, a fraction of dust particles can be elevated to the upper troposphere by orographic uplift (Zhu et al., 2022), possibly initiating in-situ heterogeneous nucleation (Kanji et al., 2017; Froyd et al., 2022; Yang et al., 2022). Although homogeneous nucleation can be effective at temperatures of < -38 °C under suitable moisture conditions, heterogeneous nucleation may inevitably take place in cirrus clouds in the presence of dust particles (Ansmann et al., 2019a; He et al., 2022a). Compared with homogeneous nucleation, the participation of heterogeneous nucleation strongly alters the microphysical properties of cirrus clouds, showing a reduction of ice crystal number concentration (ICNC) and a growth of crystal size, which thereby allows more long-wave radiation to emit to space and contributes more cooling effect to the radiation budget of Earth (Kuebbeler et al., 2014). As estimated by the simulation studies, the involvement of heterogeneous nucleation in cirrus formation would solely induce a net cloud forcing of -0.4 $W \cdot m^{-2}$ (Liu et al., 2012), -2.0 $W \cdot m^{-2}$ (Lohmann et al., 2008), or -0.94 $W \cdot m^{-2}$ (Kuebbeler et al., 2014).

60 It is also worth noting that high ice supersaturation ratios of >1.4 - 1.5 are indispensable to triggering homogeneous freezing (Koop et al., 2000; Cziczo et al., 2013). Therefore, due to the supply of surrounding dust INPs, cirrus clouds (so-called dust-related cirrus clouds here) may form via heterogeneous nucleation solely, or alternatively, via the competition between heterogeneous and homogeneous ice nucleation (Zhao et al., 2019; Zhao et al., 2022), depending on both the temperature and



ice supersaturation conditions. These two ice-nucleating mechanisms can result in quite discrepant microphysical properties
65 in cirrus clouds. However, the competition between heterogeneous and homogeneous ice nucleation is still not well understood
due to insufficient measurements (Spichtinger and Cziczo, 2010; Maloney et al., 2022; Kärcher et al., 2022). In a review report
on cirrus clouds, Heymsfield et al. (2017) pointed out that measuring/documenting the relative importance of homogeneous
versus heterogeneous nucleation of in-cloud ice crystals is considered one out of seven challenging tasks to be fulfilled in
cirrus cloud research.

70 According to the abovementioned motivations, it is necessary to identify the heterogeneous-sole and competition ice-
nucleating mechanisms of dust-related cirrus clouds. To realize this purpose, we propose to perform a closure study on the
relationship between the dust INP concentration (INPC) and ICNC (Knopf et al., 2022) on the basis of the principle that one
INP generates one ice crystal under the heterogeneous nucleation regime. It can be expected that the heterogeneous-sole case
will successfully achieve the INPC-ICNC closure, while in the competition case, the in-cloud ICNC will further exceed the
75 dust INPC attributed to the involvement of homogeneous freezing. Studies on the aerosol-cloud interaction by linking the
INPC and ICNC were first successfully attempted based on airborne in situ observations (Prenni et al., 2009; Costa et al.,
2017), and were extended to the ground-based active remote sensing approach (i.e., lidar-radar combinational observation)
later benefiting from the development of retrieval techniques of ICNC (Bühl et al., 2019) and INPC (Mamouri and Ansmann,
2014, 2015; Ansmann et al., 2019a).

80 To extend this method to a global scale, space-borne observations are necessary. Recently, the INPC-ICNC closure study
was successfully conducted with active remote sensing from space, benefitting from the reliable ICNC values provided by
DARDAR (liDAR/raDAR) product (Sourdeval et al., 2018; Gryspeerd et al., 2018), which combines the observations of
space-borne lidar and millimeter-wave radar. By comparing with in situ measurements, it has been proved that ICNC in cirrus
clouds can be reliably represented by DARDAR product (Marinou et al., 2019). Moreover, dust INPC can be retrieved from
85 space-borne lidar observation with the POLIPHON (POLarization LIDAR PHOTometer Networking) method. These two active
remote-sensing instruments are able to accurately offer the vertical-resolved information on clouds and aerosols, providing a
unique way to study the dust-cirrus interaction. In consequence, in this study, we aim to identify the specific ice-nucleating
mechanisms by comparing the ICNC in cirrus cloud provided by the DARDAR dataset with the dust INPC in the vicinity
derived by POLIPHON method. Two typical cirrus cases over central China regions, where dust plumes frequently intrude
90 during spring and winter (He et al., 2015), are shown as a demonstration of the proposed method.

The organization of this paper is as follows. First, we briefly introduce the observational data and POLIPHON method used
in the study. Then two typical case studies are presented to show the diversity of different ice-nucleating mechanisms. In the
last section, some discussions, as well as conclusions, are given.



2 Data and methodology

95 2.1 CALIOP data

To obtain the profiles of aerosol optical properties, we used the observational data from a space-borne polarization lidar, i.e., the Cloud-Aerosol Lidar with Orthogonal Polarization (CALIOP). The CALIOP instrument was carried on the Cloud-Aerosol Lidar and Infrared Pathfinder Satellite Observation (CALIPSO) launched in April 2006 (Winker et al., 2007). CALIOP has three detecting channels and thus, can measure the elastic backscatters at both 532 nm and 1064 nm and the depolarization ratio at 532 nm. In this study, the level-2 aerosol profile data product (version 4.2) was used to provide the vertical distributions of the aerosol extinction coefficient, particle depolarization ratio, and atmospheric volume description (Omar et al., 2009). The atmospheric volume description product can further give the information on the vertical feature mask (i.e., identifying cloud and aerosol), aerosol subtype, and cloud subtype.

‘Cirrus’ can be identified by cloud subtype product; ‘dust’ and ‘polluted dust’ can be identified by aerosol subtype product. Using these identifications together with the 532-nm total attenuated backscatter coefficient and volume polarization ratio (in CALIPSO level-1B data product), we can distinguish the dust-related cirrus clouds. The basic principle of case selection is that dust particles are observed closely in the vicinity (e.g., in vertical or horizontal directions) of cirrus cloud. More details about case selections can be found in He et al. (2022a).

Taking aerosol extinction coefficient α_p , particle depolarization ratio δ_p , and assumed aerosol lidar ratio into the calculation, we can obtain the dust backscatter coefficient β_d (Tesche et al., 2009) and dust extinction coefficient α_d by using a constant dust lidar ratio of 45 sr (He et al., 2021a; Peng et al., 2021). The related calculation process is given in Table 1. Then, the dust extinction coefficient α_d will be taken as the input parameter in POLIPHON calculation.

2.2 ICNC derived from DARDAR dataset

To achieve the microphysical properties of cirrus clouds, we used the DARDAR dataset, which is the output of synergistic radar-lidar retrieval (Delanoë and Hogan, 2008, 2010). The DARDAR dataset retrieves the cloud properties by combining the measurements of the CALIOP instrument on CALIPSO satellite and the 94-GHz cloud profiling radar (CPR) on CloudSat satellite (launched in April 2006 together with CALIPSO). This lidar-radar combined approach is also broadly used in ground-based observation to retrieve cloud microphysical properties (Bühl et al., 2019). Both satellites belong to NASA’s ‘A-train’ constellation and thus can realize the collocated and quasi-simultaneous measurements of aerosols and clouds. It should be mentioned that nighttime measurements for CloudSat are only available until 2011.

In this study, the DARDAR-Cloud product is employed to provide the profiles of ice cloud properties, including the cloud extinction coefficient, cloud particle effective radius (r_e), and ice water content (IWC). The DARDAR-Nice profile product is used to obtain the profiles of ice crystals number concentration n_{ice} within the clouds. The n_{ice} values with ice-crystal diameters (i.e., maximum dimension) larger than 5 μm , 25 μm , and 100 μm are respectively derived with the approach presented by Sourdeval et al. (2018) and Gryspeerdt et al. (2018), using two parameters from the DARDAR-Cloud product,



i.e., ice water content and normalization factor of the modified gamma size distribution (N_0^*). Both DARDAR-Cloud and DARDAR-Nice products have 60-m vertical and 1.7-km horizontal resolution.

The uncertainty in n_{ice} is about 25% in lidar-radar condition and 50% in lidar- or radar-only conditions. Benefitting from the better transparent condition, n_{ice} data product is considered more accurate for cirrus cloud than for mixed-phase cloud. In addition, high homogeneous nucleation rates would result in an additional 50% underestimation of n_{ice} attributed to derivations from the assumed particle size distribution (Marinou et al., 2019). Therefore, Marinou et al. (2019) stated that the DARDAR-retrieved n_{ice} can reflect the order of magnitude of the true n_{ice} . Moreover, Krämer et al. (2020) compared the n_{ice} values from the DARDAR-Nice product with the in situ measuring results from five campaigns and found that there is an overestimation within a factor of 2 for n_{ice} in DARDAR-Nice. They considered this offset for n_{ice} tolerable given the variability of 6 orders of magnitude.

2.3 INPC calculated by POLIPHON method

The dust-related INPC is estimated from the CALIOP observations in dust-existing regions in the vicinity of interesting cirrus clouds. The dust INPC is calculated with the POLIPHON method using the dust extinction coefficient as the input parameter (Tesche et al., 2009; Mamouri and Ansmann, 2015, 2016, 2017), which is separated from the CALIOP-retrieved aerosol extinction coefficient with the one-step approach reported by Mamouri and Ansmann (2014). The calculation processes of the dust-related optical and ice-nucleating parameters as well as their estimated uncertainties are given in detail in Table 1. The meteorological parameters, including the pressure and temperature, are obtained from the radiosonde measurements (Guo et al., 2019, 2020, 2021) at a meteorological station (i.e., in Wuhan city (30.5°N, 114.4°E)) in central China.

Although cirrus clouds usually occur above -38 °C isotherm, both immersion (nucleates from supercooled liquid droplet with INP immersed) and deposition (including water vapor deposits onto the insoluble surface of INP and pore condensation and freezing (PCF)) freezing modes may take place in ice nucleation in cirrus clouds (Kanji et al., 2017; Marcolli, 2014). Therefore, in the dust-INPC computation, we utilized the parameterization schemes of D10 (DeMott et al., 2010), D15 (DeMott et al., 2015), and U17-I (Ullrich et al., 2017) for immersion freezing, and U17-D (Ullrich et al., 2017) for deposition freezing. Compared with the S15 (Steinke et al., 2015) scheme, Marinou et al. (2019) found that the lidar-derived INPCs with the U17-D scheme are more coincident with those measured with unmanned aerial vehicles; thus, only U17-D scheme was applied in calculating the dust-related INPC in deposition freezing mode. For the D10 and D15 parameterizations, the dust extinction coefficient should first be converted into the particle number concentration with a radius >250 nm ($n_{250,d}$) by multiplying by a conversion factor $c_{250,d}$. The retrieval of $c_{250,d}$ for the mixed dust situation (i.e., mix with local urban aerosols) over Wuhan has been introduced in detail by He et al. (2021b). In addition, another conversion factor $c_{s,d}$ is needed to convert the dust extinction coefficient into particle surface area concentration S_d , which is the input parameter for the U17 parameterization. Using the same sun photometer dataset for $c_{250,d}$ retrieval, by selecting mixed dust cases with a ground-based polarization



lidar, we can obtain the $c_{s,d}$ of $1.99 \times 10^{-6} \text{ Mm m}^2\text{m}^{-3}$ for mixed dust situation (33 dust-intrusion days during 2011-2013) over Wuhan as shown in figure 1.

3 Observational results of two typical cirrus cloud cases

160 In principle, one INP can form one ice crystal via primary heterogeneous nucleation (Ansmann et al., 2019a); at cirrus
altitudes, secondary ice production that usually occurs at modest supercooling (temperature $\geq -10^\circ\text{C}$) can be excluded (Field et
al., 2017). A closure study means that INPC and ICNC coincide with each other well, at least within the same order of
magnitude, when ignoring collision and aggregation of ice crystals and taking the uncertainties in them into consideration
(Ansmann et al., 2019; Marinou et al., 2019; Knopf et al., 2021). Here we give two typical case studies in detail. The first case
165 realizes the closure between the dust INPC and the in-cloud ICNC, while the second case shows that the in-cloud ICNC
dramatically exceeds the dust INPC. The evident differences between two typical cases can be considered a good
demonstration to reveal the dominant ice-nucleating mechanism in cirrus cloud.

3.1 Case on 29 December 2010: sole presence of heterogeneous nucleation

Figure 2 shows the 532-nm total attenuated backscatter coefficient (TAB) and volume depolarization ratio δ_v obtained from
170 the CALIOP Level-1B data product on 15 May 2008. In both black rectangles, when the footprint of the CALIPSO satellite
passed over the region near Wuhan, three adjacent ice clouds with δ_v of >0.3 and intensive TAB (in red and gray) appeared at
altitudes of approximately 9-11 km. These clouds were observed to be embedded in a dust plume with δ_v of 0.1-0.2 and
relatively weaker TAB (in blue and yellow). Dust particles were full of the cloud-free regions on the south and north of the
cloud. The cloud top mainly overlapped with the top edges of the dust layer, indicating that dust particles may take part in
175 heterogeneous ice formation in the cloud. Therefore, these ice clouds can be considered dust-related cirrus clouds (He et al.,
2021a, 2022a). As shown in figure 3, the dust plume and cirrus cloud are confirmed to occur at altitudes of 9-11 km by the
atmospheric volume description data from the CALIOP level-2 aerosol profile product. Cirrus clouds and dust aerosols
occurred in turns (figure 3a) in the latitude range of 32-35°N, revealing the probable dust-cirrus interaction.

Figure 4 presents the ice cloud properties including the cloud extinction coefficient, cloud particle effective radius, and ice
180 water content from the DARDAR-Cloud product on 15 May 2008 (the same time and location as figures 2 and 3). It is noticed
that the cirrus clouds above ~ 9 km generally show a smaller extinction coefficient ($<1.0 \text{ km}^{-1}$) and particle size ($<50 \mu\text{m}$) than
those altocumulus and altostratus at lower altitudes. Taking the cirrus cloud at altitudes of 9-11 km and latitudes of 33.2-
35.0°N into calculation, the in-cloud averaging extinction coefficient, cloud particle effective radius, and ice water content are
0.47 km^{-1} , 35.48 μm , and 10.99 mg m^{-3} , respectively.

185 The CALIOP profiles in the cloud-free regions nearby (32.0-33.2°N) are integrated to estimate the INPCs related to the
cirrus cloud. The aerosol extinction coefficient and backscatter coefficient for total (dust + non-dust) and dust composition as
well as particle depolarization ratio δ_p are presented in figure 5. Above 9 km, two distinct dust layers appeared at 9.0-9.8 km



and 10.6-10.9 km, respectively, both with a peak δ_p of around 0.3. These dust layers also contained some non-dust components as seen from their contributions to the total extinction and backscatter coefficients (figures 5a and 5b), which can also be verified by the aerosol subtype of ‘polluted dust’ (in brown, see figure 3c). For the upper layer (10.6-10.9 km), the layer-averaged dust extinction coefficient was 13.0 Mm^{-1} ; while for the lower-lying layer (at 9.0-9.8 km), the layer-averaged dust extinction coefficient was 13.6 Mm^{-1} . These dust layers were related to the heterogeneous ice nucleation in the cirrus cloud at altitudes of 9-11 km.

Figure 6 shows the concentration profiles of the dust mass, large particle number (with radius $>250 \text{ nm}$), and surface area calculated from the dust extinction (see figure 5). The dust-related INPC profiles can be obtained in turn. At temperatures warmer than $-35 \text{ }^\circ\text{C}$, immersion heterogeneous freezing was considered in INPC calculation with the parameterization schemes of D10, D15, and U17-I (immersion freezing for dust particles). Contacting freezing, which needs an INP to collide with a supercooled droplet, was less likely to occur and thus was ignored here (Hoffmann et al., 2013; Ansmann et al., 2019a). At temperatures above $-35 \text{ }^\circ\text{C}$ isotherm, the INPC for deposition freezing was calculated with the U17-D (for dust particles) parameterization which has an applicable temperature range of -33 – $-67 \text{ }^\circ\text{C}$. For the upper dust layer at altitudes of 10.6-10.9 km, the averaging dust-related INPCs are 0.405 L^{-1} (0.042 - 0.931 L^{-1}) for U17-D with S_i of 1.15, 9.897 L^{-1} (0.891 - 23.875 L^{-1}) for U17-D with S_i of 1.25, and 102.792 L^{-1} (8.341 - 256.571 L^{-1}) for U17-D with S_i of 1.35. For the lower dust layer at altitudes of 9.0-9.8 km, the averaging dust-related INPCs are 0.003 L^{-1} (0 - 0.007 L^{-1}) for U17-D with S_i of 1.15, 0.041 L^{-1} (0.001 - 0.083 L^{-1}) for U17-D with S_i of 1.25, and 0.259 L^{-1} (0.010 - 0.527 L^{-1}) for U17-D with S_i of 1.35.

The number concentrations of ice crystals larger than $5 \mu\text{m}$, $25 \mu\text{m}$, and $100 \mu\text{m}$ from the DARDAR-Nice product are shown in figure 6c. Here we denote these three types of ICNC values as $n_{\text{ice},5\mu\text{m}}$, $n_{\text{ice},25\mu\text{m}}$, and $n_{\text{ice},100\mu\text{m}}$, respectively. The averaging ICNCs within the upper part of cirrus clouds at altitudes of 10.6-10.9 km (corresponding to the lower dust layer) are 121.8 L^{-1} (108.3 - 140.4 L^{-1}) for $n_{\text{ice},5\mu\text{m}}$, 59.1 L^{-1} (51.1 - 70.6 L^{-1}) for $n_{\text{ice},25\mu\text{m}}$, and 11.7 L^{-1} (8.2 - 15.8 L^{-1}) for $n_{\text{ice},100\mu\text{m}}$, respectively. It is of great interest to note that the INPCs retrieved by U17-D with S_i of 1.35 are in good agreement with the in-cloud $n_{\text{ice},5\mu\text{m}}$ (ICNC / INPC ratio is 1.2) and $n_{\text{ice},25\mu\text{m}}$ (ICNC / INPC ratio is 0.6) within this thin vertical extent (10.6-10.9 km) near the cloud top, where the initiation of ice formation usually takes place. While the INPCs retrieved by U17-D with S_i of 1.25 are closer to the in-cloud $n_{\text{ice},100\mu\text{m}}$ (ICNC / INPC ratio is 1.2). These INPC-ICNC relationships show a good match within an order of magnitude, which thus can be considered successful closure. Moreover, the typical ICNCs for heterogeneous freezing are reported to be 1 - 100 L^{-1} by Cziczo et al. (2013) and 4.3 - 39 L^{-1} by Ansmann et al. (2019a) (for the thin cirrus case therein), which are generally consistent with the observation in this case. Therefore, it can be concluded that heterogeneous nucleation solely occurred within the upper part of cirrus clouds, which is also explained by the plunge of ICNC at this altitude range.

For the lower part of cirrus clouds (9.0-9.8 km), the layer-averaging ICNCs are 186.8 L^{-1} (129.8 - 233.1 L^{-1}) for $n_{\text{ice},5\mu\text{m}}$, 86.7 L^{-1} (60.8 - 106.7 L^{-1}) for $n_{\text{ice},25\mu\text{m}}$, and 11.2 L^{-1} (8.5 - 12.4 L^{-1}) for $n_{\text{ice},100\mu\text{m}}$, respectively. The ICNCs at these altitudes are much larger than those within the upper part of clouds (10.6-10.9 km). The ICNC values are 2-3 orders of magnitude larger



than the corresponding INPC values at the same altitudes. These large ICNCs are possibly attributed to both ice crystals falling from above (He et al., 2022b) and the occurrence of homogeneous nucleation. Consequently, competition between heterogeneous and homogeneous nucleation also took place in the lower part of cirrus clouds. Additionally, at warmer altitudes of 8–9 km (with temperatures of -27 – -35 °C), the successful closures were also realized for the immersion freezing mode, as seen from the relationships of $n_{\text{ice},100\mu\text{m}}$ –INPC (D10), $n_{\text{ice},25\mu\text{m}}$ –INPC(D15), and $n_{\text{ice},5\mu\text{m}}$ –INPC(D15).

3.2 Case on 31 December 2010: competition between heterogeneous and homogeneous nucleation

Another case was observed on 31 December 2010. Figure 7 shows the altitude-orbit contour plots of the 532-nm total attenuated backscatter coefficient and volume depolarization ratio δ_v . The black rectangles mark a thick cirrus cloud extending from an altitude of 5 km to up to 10 km, with intense TAB (in gray and red) and enhanced δ_v of 0.2–0.4. Meanwhile, dust aerosols were observed in the vicinity of the cirrus cloud. The dust plume overall showed a wide horizontal extent within the latitudes of 22–33°N, presenting a descent trend from north to south along with the crossing path. For the cirrus cloud, a similar north-south height gradient was observed, suggesting the relationship between the cloud formation and dust particles. Moreover, the presence of the cirrus cloud and dust plume can also be verified by the simultaneous cloud subtype and aerosol subtype data from the CALIOP Level-2 product (see figure 8).

The ice cloud properties, i.e., the cloud extinction coefficient, cloud particle effective radius, and ice water content, on 31 December 2010 provided by the DARDAR-Cloud product are represented in figure 9. The time and location for the measurement are the same as those in figures 7 and 8). Taking the cirrus cloud at altitudes of 5–10 km and latitudes of 33–35°N into calculation, the in-cloud averaging extinction coefficient, cloud particle effective radius, and ice water content are 0.49 km^{-1} , 46.55 μm , and 14.77 mg m^{-3} , respectively.

The cloud-free CALIOP profiles in central China (31.3–32.5°N) are integrated to estimate the dust extinction coefficient and in turn, the INPC near the cirrus cloud. Figure 10 shows the aerosol extinction coefficient and backscatter coefficient for total (dust + non-dust) and dust composition, and the particle depolarization ratio δ_p . Two distinct dust layers can be seen clearly. The upper dust layer was located at altitudes of 8.5–9.6 km with a peak δ_p exceeding 0.3, revealing the presence of pure dust particles. Within this dust layer, dust extinction contributed the most proportion of total aerosol extinction; the layer-averaged dust extinction coefficient reached up to 21.2 Mm^{-1} , with a peak value of 56.9 Mm^{-1} at around 8.9 km. As for the lower-lying dust layer at altitudes of 5.0–6.8 km, the layer-averaged dust extinction coefficient was 12.3 Mm^{-1} , nearly a half compared with that for the upper layer; the maximum value was 23.9 Mm^{-1} at an altitude of 5.7 km. Considering that the vertical extent of the cirrus cloud (5–10 km) and dust layers (i.e., 5.0–6.8 km and 8.5–9.6 km) are partly overlapped, dust particles possibly participated in the heterogeneous ice formation in the cirrus cloud (at least for the lower part of cloud), which will be further analyzed by comparing the dust-related INPC and ICNC within the cloud.

To examine the possible nucleation mechanism, the profiles of dust mass concentration, large particle (with radius >250 nm) number concentration, surface area, dust-related INPC, and in-cloud ICNC are calculated as presented in figure 11. For the



lower-lying dust layer, the temperature lay in a warm range of >-25 °C, meaning that heterogeneous nucleation solely took place. To obtain the dust-related INPC, the parameterization schemes of D10, D15, and U17-I for immersion mode were taken
255 into calculation. U17-I shows the best performance according to the comparison with $n_{ice,100\mu m}$. As for the upper dust layer, the temperature ranged from -35 °C to -40 °C; thus, the parameterization U17-D for deposition freezing was applied to compute the INPC. Ice saturation ratio values S_i were assumed to be 1.15, 1.25, and 1.35, respectively. A larger ice saturation ratio resulted in more active INPs. For the upper dust layer at altitudes of 8.5-9.6 km, the averaging dust-related INPCs are 0.016 L^{-1} (0.002 - 0.043 L^{-1}) for U17-D with S_i of 1.15, 0.232 L^{-1} (0.028 - 0.641 L^{-1}) for U17-D with S_i of 1.25, and 1.667 L^{-1} (0.202 -
260 4.672 L^{-1}) for U17-D with S_i of 1.35.

The averaging ICNCs within the upper part of the cirrus cloud (corresponding to the upper dust layer at 8.5-9.6 km) are 93.4 L^{-1} (59.8 - 129.7 L^{-1}) for $n_{ice,5\mu m}$, 44.2 L^{-1} (27.5 - 62.1 L^{-1}) for $n_{ice,25\mu m}$, and 6.6 L^{-1} (3.4 - 9.6 L^{-1}) for $n_{ice,100\mu m}$, respectively. The maximum $n_{ice,5\mu m}$ reaches up to 129.7 L^{-1} . As reviewed by Heymsfield et al. (2017), the cirrus total ice concentrations generally fall in the range of 5 - 500 L^{-1} . However, based on a simulation study, Liu et al. (2012) found that the ICNCs in cirrus
265 clouds are 100 - 300 L^{-1} in the subtropical and mid-latitudes of the Northern Hemisphere, which is attributed to the coexistence of homogeneous and heterogeneous (associated with the Saharan and Asian dust) nucleation. They concluded that heterogeneous nucleation may deplete water vapor supply within the cloud parcel and further inhibit homogeneous nucleation, resulting in a decreasing number of ice crystals. Compared with the typical ICNC of >300 L^{-1} for pure homogeneous freezing, the in-cloud ICNCs are relatively smaller in this case, caused by the combination of homogeneous and heterogeneous
270 nucleation (Kärcher et al., 2022).

The ICNCs containing smaller ice crystals (i.e., $n_{ice,5\mu m}$ and $n_{ice,25\mu m}$) are more than an order of magnitude larger than the dust-related INPCs with S_i of 1.35 (ICNC / INPC ratios are 55.9 and 26.5, respectively), indicating that a great number of small-size ice crystals were formed via homogeneous nucleation (Liu et al., 2012; Cziczo et al., 2013). The $n_{ice,100\mu m}$ values are more comparable to these INPCs ($S_i = 1.35$) within an order of magnitude (ICNC / INPC ratio is 3.9), especially at ~ 9.5
275 km where $n_{ice,100\mu m}$ is substantially consistent with INPC, suggesting the participation of heterogeneous nucleation that usually produces ice crystals with large size and small number concentration (Cziczo et al., 2013). Therefore, we can conclude that heterogeneous and homogeneous nucleation took place simultaneously, competing for water vapor. Under this competition situation, heterogeneous nucleation would gradually be dominant along with the consumption of water vapor, because the ambient relative humidity with respect to ice would continually decline (He et al., 2022a). Haag et al. (2003) reported that the combination of homogeneous and heterogeneous nucleation may probably take responsibility for the in-situ formation of cirrus
280 clouds in the mid-latitude regions of the Northern Hemisphere. The in-situ measurements by DeMott et al. (2003) also supported the conclusion that cirrus formation can occur both by heterogeneous nucleation by insoluble particles (i.e., ice-nucleating particles) and homogeneous freezing of particles containing solutions.



4 Discussions and conclusions

285 We propose a method to identify two ice-nucleating mechanisms of dust-related cirrus clouds based on space-borne observations (He et al., 2022a; Kärcher et al., 2022): (1) sole presence of heterogeneous nucleation; (2) competition between heterogeneous and homogeneous nucleation. To distinguish the two mechanisms, the basic thought is to compare the ICNC within a cirrus cloud with the dust-related INPC in the vicinity. The in-cloud ICNC data are obtained from the DARDAR dataset (Sourdeval et al., 2018) upon the synergistic observations of CALIPSO and CloudSat satellites. The dust-related INPC
290 is derived with the POLIPHON method using the observational data from the space-bore lidar CALIOP on CALIPSO satellite (Mamouri and Ansmann, 2014, 2015, 2016, 2017; Marinou et al., 2019; Ansmann et al., 2019b). We consider the deposition freezing and immersion freezing herein.

In this study, two typical cases corresponding to the abovementioned ice-nucleating mechanisms are studied in detail as a demonstration (see table 2). Both cases are observed in central China. The conversion factors obtained in Wuhan city (30.5°N,
295 114.4°E) are applied in POLIPHON calculation (He et al., 2021b). For the heterogeneous-sole case, the estimated INPC and ICNC values generally realize successful closure within the upper part of cirrus clouds, i.e., they generally are in good agreement within an order of magnitude (Ansmann et al., 2019a), indicating the ice formation rule that one ice-nucleating particle generates one ice crystal by heterogeneous nucleation. For the competition case, the estimated ICNCs dramatically exceed the INPCs for more than an order of magnitude, which can even reach up to several orders of magnitude, meaning that
300 homogeneous nucleation is involved in ice formation and additionally produces a surging number of ice crystals.

A conceptual sketch of two ice-nucleating mechanisms is shown in figure 12. The heterogeneous-sole situation is generally composed of fewer ice crystals with large size, allowing more solar radiation to enter the atmosphere and emitting less long-wave radiation back to space. In contrast, the competition situation probably leads to an optically denser cirrus cloud containing numerous smaller ice crystals produced by homogeneous nucleation, reflecting a large proportion of solar radiation back to
305 space and inhibiting more long-wave radiation from emitting back to space (DeMott et al., 2010; Kuebbeler et al., 2014).

Considering the integration of incoming solar radiation and outgoing long-wave radiation, unseeded cirrus clouds are traditionally considered to result in a net warming effect on Earth's atmosphere ($5.7 \text{ W}\cdot\text{m}^{-2}$ as given by Gasparini and Lohmann, 2016). However, the diversity of cirrus-formation regimes induces a vital source of uncertainties in Earth's radiation budget as well as in weather and climate predictions (Kienast-Sjögren et al., 2016). Spichtinger and Cziczo (2009) mentioned that
310 both net warming induced by thin cirrus clouds and net cooling by thick cirrus clouds are possible to occur. Fusina et al. (2007) reported that under certain conditions ice crystal number concentrations play a crucial role in the transition between net warming and cooling. In recent years, there has been rising a new concept, i.e., 'cirrus cloud thinning', in light of the assumption that more cirrus clouds nucleate via heterogeneous freezing. It is even under discussion that cirrus clouds thinning can offset current climate warming (Lohmann and Gasparini, 2017). The proposed method herein may be conducive to
315 understanding the potential effect of cirrus cloud thinning.



By comparing the ICNC and INPC, this study presents a demonstration of ice-nucleating regimes identification for the dust-related cirrus clouds. However, there are still many efforts needed to pay. In the future, a long-term study will be conducted with the high-quality DARDAR product during 2006-2010, when the simultaneous nighttime observations of CloudSat and CALIPSO are available. In addition, we selected the central China region to provide an exemplary observation; benefiting from the space-borne observations, such a study is expected to extend to a global scale so that it can potentially offer constructive suggestions of cirrus representation to the current climate mode (Froyd et al., 2022; Maloney et al., 2022). To realize this goal, regional POLIPHON conversion factors shall be retrieved using sun photometer data from not only global AERONET (Holben et al., 1998; Ansmann et al., 2019b) but also some other regional networks, such as SONET (Sun-sky radiometer Observation NETWORK, Li et al., 2018), CARSONET (China Aerosol Remote Sensing Network, Che et al., 2009), and SKYNET (Sky Radiometer Network, Nakajima et al., 2007), to cover more diverse aerosol types and complete aerosol optical/microphysical properties along the long-range transport path. Moreover, the proposed method using the measurement data from space is based on the ‘snapshot’ observation; to validate its reliability and realize a process-level observation, intercomparison with simultaneous ground-based observations using the same approach as well as with in-situ measurements conducted by aircraft are also necessary. These efforts will improve our inadequate understanding of the impact of upper-troposphere dust on global climate (Yang et al., 2022; Zhu et al., 2022).

Data availability

Sun photometer data used to generate the results of this paper are available at the website (doi:10.5281/zenodo.4683015). CALIPSO data used in this work can be accessed through the website <https://subset.larc.nasa.gov>. Radiosonde data can be obtained at the following website <http://weather.uwyo.edu/upperair/sounding.html>. DARDAR products are at the website <https://www.icare.univ-lille.fr>.

Author Contributions

Yun He conceived the research, analyzed the data, acquired the research funding, and wrote the manuscript. Zhenping Yin analyzed the data, participated in the scientific discussions, and reviewed and proofread the manuscript. Fuchao Liu reviewed and proofread the manuscript. Fan Yi acquired the research funding and led the study.

Competing interests

The authors declare that they have no conflict of interest.



Acknowledgments

This work is supported by the National Natural Science Foundation of China (grant nos. 42005101 and 41927804), the Hubei Provincial Natural Science Foundation of China (grant no. 2020CFB229), the Fundamental Research Funds for the Central Universities (grant nos. 2042020kf0018 and 2042021kf1066), and the Meridian Space Weather Monitoring Project (China). The authors thank the University of Wyoming for providing the radiosonde data, the Atmospheric Science Data Central (ASDC) at the NASA Langley Research Center for providing the CALIPSO data, the ICARE Thematic Center for generating and storing the DARDAR products.

References

- 350 Ansmann, A., Mamouri, R.-E., Bühl, J., Seifert, P., Engelmann, R., Hofer, J., Nisantzi, A., Atkinson, J. D., Kanji, Z. A., Sierau, B., Vrekoussis, M., and Sciare, J.: Ice-nucleating particle versus ice crystal number concentration in altocumulus and cirrus embedded in Saharan dust: A closure study, *Atmos. Chem. Phys.*, 19, 15087-15115. doi.org/10.5194/acp-19-15087-2019, 2019a.
- Ansmann, A., Mamouri, R.-E., Hofer, J., Baars, H., Althausen, D., and Abdullaev, S. F.: Dust mass, cloud condensation nuclei, and ice-nucleating particle profiling with polarization lidar: updated POLIPHON conversion factors from global AERONET analysis, *Atmos. Meas. Tech.*, 12, 4849-4865. doi.org/10.5149/amt-12-4849-2019, 2019b.
- Ansmann, A., Ohneiser, K., Mamouri, R.-E., Knopf, D. A., Veselovskii, I., Baars, H., Engelmann, R., Foth, A., Jimenez, C., Seifert, P., and Barja, B.: Tropospheric and stratospheric wildfire smoke profiling with lidar: mass, surface area, CCN, and INP retrieval, *Atmos. Chem. Phys.*, 21, 9779-9807, doi.org/10.5194/acp-21-9779-2021, 2021.
- 360 Bühl, J., Seifert, P., Radenz, M., Baars, H., and Ansmann, A.: Ice crystal number concentration from lidar, cloud radar and radar wind profiler measurements, *Atmos. Meas. Tech.*, 12, 6601-6617, doi.org/10.5194/amt-12-6601-2019, 2019.
- Che, H., Zhang, X., Chen, H., Damiri, B., Goloub, P., Li, Z., Zhang, X., Wei, Y., Zhou, H., Dong, F., Li, D., and Zhou, T.: Instrument calibration and aerosol optical depth validation of the China Aerosol Remote Sensing Network, *J. Geophys. Res.*, 114, D03206, doi.org/10.1029/2008JD011030, 2009.
- 365 Costa, A., Meyer, J., Afchine, A., Luebke, A., Günther, G., Dorsey, J. R., Gallagher, M. W., Ehrlich, A., Wendisch, M., Baumgardner, D., Wex, H., and Krämer, M.: Classification of Arctic, midlatitude and tropical clouds in the mixed-phase temperature regime, *Atmos. Chem. Phys.*, 17, 12219-12238, doi.org/10.5194/acp-17-12219-2017, 2017.
- Cziczo, D., Froyd, K., Hoose, C., Jensen, E., Diao, M., Zondlo, M., Smith, J., Twohy, C., and Murphy, D.: Clarifying the dominant sources and mechanisms of cirrus cloud formation, *Science*, 340, 1320-1324, doi.org/10.1126/science.1234145, 370 2013.
- Delanoë, J., and Hogan, R. J.: A variational scheme for retrieving ice cloud properties from combined radar, lidar, and infrared radiometer, *J. Geophys. Res.*, 113, D07204, doi.org/10.1029/2007JD009000, 2008.



- Delanoë, J., and Hogan, R. J.: Combined CloudSat-CALIPSO-MODIS retrievals of the properties of ice clouds, *J. Geophys. Res.*, 115, D00H29, doi.org/10.1029/2009JD012346, 2010.
- 375 DeMott, P., Cziczo, D., Prenni, A., Murphy, D., Kreidenweis, S., Thomson, D., Borys, R., and Rogers, D.: Measurements of the concentration and composition of nuclei for cirrus formation, *P. Natl. Acad. Sci. USA*, 100, 14655-14660. doi.org/10.1073/pnas.2532677100, 2003.
- DeMott, P., Prenni, A., Liu, X., Kreidenweis, S., Petters, M., Twohy, C., Richardson, M., Eidhammer, T., and Rogers, D.: Predicting global atmospheric ice nuclei distributions and their impacts on climate, *P. Natl. Acad. Sci. USA*, 107, 11217-11222. doi.org/10.1073/pnas.0910818107, 2010.
- 380 DeMott, P., Prenni, A., McMeeking, G., Sullivan, R., Petters, M., Tobo, Y., Niemand, M., Möhler, O., Snider, J., Wang, Z., and Kreidenweis, S.: Integrating laboratory and field data to quantify the immersion freezing ice nucleation activity of mineral dust particles, *Atmos. Chem. Phys.*, 15, 393-409. doi.org/10.5194/acp-15-393-2015, 2015.
- Field, P., Lawson, P., Brown, G., Lloyd, C., Westbrook, D., Moisseev, A., Miltenberger, A., Nenes, A., Blyth, A., Choulaton, T., Connolly, P., Bühl, J., Crosier, J., Cui, Z., Dearden, C., DeMott, P., Flossmann, A., Heymsfield, A., Huang, Y., Kalesse, H., Kanji, Z., Korolev, A., Kirchgaessner, A., Lasher-Trapp, S., Leisner, T., McFarquhar, G., Phillips, V., Stith, J., and Sullivan, S.: Secondary ice production – current state of the science and recommendations for the future, *Meteorol. Mon.*, 58, 7.1–7.20, doi.org/10.1175/AMSMONOGRAPHS-D-16-0014.1, 2017.
- 390 Froyd, K. D., Yu, P., Schill, G. P., Brock, C. A., Kupc, A., Williamson, C. J., Jensen, E. J., Ray, E., Rosenlof, K. H., Bian, H., Darmenov, A. S., Colarco, P. R., Diskin, G. S., Bui, T., and Murphy, D. M.: Dominant role of mineral dust in cirrus cloud formation revealed by global-scale measurements, *Nat. Geosci.* 15, 177–183, doi.org/10.1038/s41561-022-00901-w, 2022.
- Fusina, F., Spichtinger, P., and Lohmann, U.: The impact of ice supersaturated regions and thin cirrus on radiation in the midlatitudes, *J. Geophys. Res.*, 112, D24S14, doi:10.1029/2007JD008449, 2007.
- 395 Gasparini, B., and Lohmann, U.: Why cirrus cloud seeding cannot substantially cool the planet, *J. Geophys. Res.-Atmos.*, 121, 4877–4893, doi.org/10.1002/2015JD024666, 2016.
- Gryspeerd, E., Sourdeval, O., Quaas, J., Delanoë, J., and Kühne, P.: Ice crystal number concentration estimates from lidar-radar satellite retrievals. Part 2: Controls on the ice crystal number concentration, *Atmos. Chem. Phys.*, doi.org/10.5194/acp-2018-21, 2018.
- 400 Ge, J., Zheng, C., Xie, H., Xin, Y., Huang, J., and Fu, Q.: Midlatitude cirrus clouds at the SACOL site: Macrophysical properties and large-scale atmospheric states, *J. Geophys. Res.-Atmos.*, 123, 2256–2271, doi.org/10.1002/2017JD027724, 2018.
- Guo, J., Lou, M., Miao, Y., Wang, Y., Zeng, Z., Liu, H., He, J., Xu, H., Wang, F., Min, M., and Zhai, P.: Trans-Pacific transport of dust aerosol originated from East Asia: Insights gained from multiple observations and modeling, *Environ. Pollut.*, 230, 1030–1039, doi.org/10.1016/j.envpol.2017.07.062, 2017.
- 405



- Guo, J., Li, Y., Cohen, J. B., Li, J., Chen, D., Xu, H., Liu, L., Yin, J., Hu, K., and Zhai, P.: Shift in the temporal trend of boundary layer height in China using long-term (1979–2016) radiosonde data, *Geophys. Res. Lett.*, 46, 6080–6089, doi.org/10.1029/2019GL082666, 2019.
- 410 Guo, J., Chen, X., Su, T., Liu, L., Zheng, Y., Chen, D., Li, J., Xu, H., Lv, Y., He, B., Li, Y., Hu, X., Ding, A., and Zhai, P.: The Climatology of Lower Tropospheric Temperature Inversions in China from Radiosonde Measurements: Roles of Black Carbon, Local Meteorology, and Large-Scale Subsidence, *J. Climate*, 33, 9327–9350, doi.org/10.1175/jcli-d-19-0278.1, 2020.
- 415 Guo, J., Zhang, J., Yang, K., Liao, H., Zhang, S., Huang, K., Lv, Y., Shao, J., Yu, T., Tong, B., Li, J., Su, T., Yim, S. H. L., Stoffelen, A., Zhai, P., and Xu, X.: Investigation of near-global daytime boundary layer height using high-resolution radiosondes: first results and comparison with ERA5, MERRA-2, JRA-55, and NCEP-2 reanalyses, *Atmos. Chem. Phys.*, 21, 17079–17097, doi.org/10.5194/acp-21-17079-2021, 2021.
- Haag, W., Kärcher, B., Ström, J., Minikin, A., Lohmann, U., Ovarlez, J., and Stohl, A.: Freezing thresholds and cirrus cloud formation mechanisms inferred from in situ measurements of relative humidity, *Atmos. Chem. Phys.*, 3, 1791–1806, doi.org/10.5194/acp-3-1791-2003, 2003.
- 420 He, Y., and Yi, F.: Dust aerosols detected using a ground-based polarization lidar and CALIPSO over Wuhan (30.5N, 114.4E), China, *Adv. Meteorol.*, Article ID 536762. doi.org/10.1155/2015/536762, 2015.
- He, Y., Yi, F., Yi, Y., Liu, F., and Zhang, Y.: Heterogeneous nucleation of midlevel cloud layer influenced by transported Asian dust over Wuhan (30.5°N, 114.4°E), China, *J. Geophys. Res.-Atmos.*, 126(2), e2020JD033394. doi.org/10.1029/2020JD033394, 2021a.
- 425 He, Y., Zhang, Y., Liu, F., Yin, Z., Yi, Y., Zhan, Y., and Yi, F.: Retrievals of dust-related particle mass and ice-nucleating particle concentration profiles with ground-based polarization lidar and sun photometer over a megacity in central China, *Atmos. Meas. Tech.*, 14, 5939–5954. doi.org/10.5194/amt-14-5939-2021, 2021b.
- He, Y., Yi, F., Liu, F., Yin, Z., and Zhou, J.: Ice nucleation of cirrus clouds related to the transported dust layer observed by ground-based lidars over Wuhan, China, *Adv. Atmos. Sci.*, doi.org/10.1007/s00376-021-1192-x, 2022a.
- 430 He, Y., Yi, F., Liu, F., Yin, Z., Yang, Y., Zhou, J. Yu, C., and Zhang, Y.: Natural seeder-feeder process originating from mixed-phase clouds observed with polarization lidar and radiosonde at a mid-latitude plain site, *J. Geophys. Res.-Atmos.*, 127(5), e2021JD036094. doi.org/10.1029/2021JD036094, 2022b.
- 435 Heymsfield, A. J., Krämer, M., Luebke, A., Brown, P., Cziczko, D. J., Franklin, C., Lawson, P., Lohmann, U., McFarquhar, G., Ulanowski, Z., and Van Tricht, K.: Cirrus clouds, *Meteorol. Mon.*, 58, 2.1-2.26, doi.org/10.1175/AMSMONOGRAPHS-D-16-0010.1, 2017.
- Hoffmann, N., Kiselev, A., Rzesanke, D., Duft, D., and Leisner, T.: Experimental quantification of contact freezing in an electrodynamic balance, *Atmos. Meas. Tech.*, 6, 2373–2382, doi.org/10.5194/amt-6-2373-2013, 2013.



- Holben, B., Eck, T., Slutsker, I., Tanré, D., Buis, J., Setzer, A., Vermote, E., Reagan, J., Kaufman, Y., Nakajima, T., Lavenu, F., Jankowiak, I., and Smirnov, A.: AERONET—A federated instrument network and data archive for aerosol characterization, *Remote Sens. Environ.* 66(1), 1-16. doi.org/10.1016/s0034-4257(98)00031-5, 1998.
- 440 Hu, Q., Goloub, P., Veselovskii, I., and Podvin, T.: The characterization of long-range transported North American biomass burning plumes: what can a multi-wavelength Mie–Raman-polarization-fluorescence lidar provide?, *Atmos. Chem. Phys.*, 22, 5399–5414, doi.org/10.5194/acp-22-5399-2022, 2022.
- IPCC, 2013: *Climate Change 2013: The Physical Science Basis. Contribution of Working Group I to the Fifth Assessment Report of the Intergovernmental Panel on Climate Change.* Cambridge University Press.
- 445 Jensen, E., Diskin, G., Lawson, R., Lance, S., Bui, T., Hlavka, D., McGill, M., Pfister, L., Toon, O., and Gao, R.: Ice nucleation and dehydration in the tropical tropopause layer, *P. Natl. Acad. Sci. USA*, 110(6), 2041-2046, doi.org/10.1073/pnas.1217104110, 2013.
- Kanji, Z. A., Ladino, L. A., Wex, H., Boose, Y., Burkert-Kohn, M., Cziczo, D. J., and Krämer, M.: Overview of ice nucleating particles, *Meteorol. Mon.*, 58, 1.1-1.33, doi.org/10.1175/AMSMONOGRAPHIS-D-16-0006.1, 2017.
- 450 Kärcher, B., DeMott, P. J., Jensen, E. J., and Harrington, J. Y.: Studies on the competition between homogeneous and heterogeneous ice nucleation in cirrus formation, *J. Geophys. Res.-Atmos.*, 127(3), e2021JD035805. doi.org/10.1029/2021JD035805, 2022.
- Kienast-Sjögren, E., Rolf, C., Seifert, P., Krieger, U. K., Luo, B. P., Krämer, M., and Peter, T.: Climatological and radiative properties of midlatitude cirrus clouds derived by automatic evaluation of lidar measurements, *Atmos. Chem. Phys.*, 16, 7605–7621, https://doi.org/10.5194/acp-16-7605-2016, 2016.
- Knopf, D. A., Barry, K. R., Brubaker, T. A., Jahl, L. G., Jankowski, K. A., Li, J., Lu, Y., Monroe, L. W., Moore, K. A., Rivera-Adorno, F. A., Saucedo, K. A., Shi, Y., Tomlin, J. M., Vepuri, H. S. K., Wang, P., Lata, N. N., Levin, E. J. T., Creamean, J. M., Hill, T. C. J., China, S., Alpert, P. A., Moffet, R. C., Hiranuma, N., Sullivan, R. C., Fridlind, A. M., West, M., 460 Riemer, N., Laskin, A., DeMott, P. J., and Liu, X.: Aerosol–ice formation closure: A Southern Great Plains field campaign, *Bull. Am. Meteorol. Soc.*, 102, E1952-E1971, doi.org/10.1175/BAMS-D-20-0151.1, 2021.
- Koop, T., Luo, B. P., Tsias, A., and Peter, T.: Water activity as the determinant for homogeneous ice nucleation in aqueous solutions. *Nature*, 406, 611–614, doi.org/10.1038/35020537, 2000.
- Krämer, M., Schiller, C., Afchine, A., Bauer, R., Gensch, I., Mangold, A., Schlicht, S., Spelten, N., Sitnikov, N., Borrmann, S., de Reus, M., and Spichtinger, P.: Ice supersaturations and cirrus cloud crystal numbers, *Atmos. Chem. Phys.*, 9, 3505–3522, doi.org/10.5194/acp-9-3505-2009, 2009.
- Krämer, M., Rolf, C., Luebke, A., Afchine, A., Spelten, N., Costa, A., Meyer, J., Zöger, M., Smith, J., Herman, R. L., Buchholz, B., Ebert, V., Baumgardner, D., Borrmann, S., Klingebiel, M., and Avallone, L.: A microphysics guide to cirrus clouds – Part 1: Cirrus types, *Atmos. Chem. Phys.*, 16, 3463-3483, doi.org/10.5194/acp-16-3463-2016, 2016.
- 470 Krämer, M., Rolf, C., Spelten, N., Afchine, A., Fahey, D., Jensen, E., Khaykin, S., Kuhn, T., Lawson, P., Lykov, A., Pan, L., Riese, M., Rollins, A., Stroh, F., Thornberry, T., Wolf, V., Woods, S., Spichtinger, P., Quaas, J., and Sourdeval, O.: A



- microphysics guide to cirrus—part 2: climatologies of clouds and humidity from observations, *Atmos. Chem. Phys.* **20**, 12569–12608, doi.org/10.5194/acp-20-12569-2020, 2020.
- 475 Kuebbeler, M., Lohmann, U., Hendricks, J., and Kärcher, B.: Dust ice nuclei effects on cirrus clouds, *Atmos. Chem. Phys.*, **14**, 3027–3046, doi.org/10.5194/acp-14-3027-2014, 2014.
- Lohmann, U., and Gasparini, B.: A cirrus cloud climate dial? *Science*, **357**(6348), 248–249, doi.org/10.1126/science.aan3325, 2017.
- 480 Li, Z. Q., Xu, H., Li, K. T., Li, D. H., Xie, Y. S., Li, L., Zhang, Y., Gu, X. F., Zhao, W., Tian, Q. J., Deng, R. R., Su, X. L., Huang, B., Qiao, Y. L., Cui, W. Y., Hu, Y., Gong, C. L., Wang, Y. Q., Wang, X. F., Wang, J. P., Du, W. B., Pan, Z. Q., Li, Z. Z., and Bu, D.: Comprehensive study of optical, physical, chemical, and radiative properties of total columnar atmospheric aerosols over China: an overview of Sun–Sky Radiometer Observation Network (SONET) measurements, *B. Am. Meteorol. Soc.*, **99**, 739–755, doi.org/10.1175/bams-d-17-0133.1, 2018.
- Liu, X., Shi, X., Zhang, K., Jensen, E., Gettelman, A., Barahona, D., Nenes, A., and Lawson, P.: Sensitivity studies of dust ice nuclei effect on cirrus clouds with the Community Atmosphere Model CAM5, *Atmos. Chem. Phys.*, **12**, 12061–12079, doi.org/10.5194/acp-12-12061-2012, 2012.
- 485 Lohmann, U., Spichtinger, P., Jess, S., Peter, T., and Smit, H.: Cirrus cloud formation and ice supersaturated regions in a global climate model. *Environ. Res. Lett.*, **3**, 045022, doi.org/10.1088/1748-9326/3/4/045022, 2008.
- Maloney, C., Toon, B., Bardeen, C., Yu, P., Froyd, K., Kay, J., and Woods, S.: The balance between heterogeneous and homogeneous nucleation of ice clouds using CAM5/CARMA, *J. Geophys. Res.-Atmos.*, **127**(6), e2021JD035540, doi.org/10.1029/2021JD035540, 2022
- 490 Mamouri, R. E. and Ansmann, A.: Fine and Coarse dust separation with polarization lidar, *Atmos. Meas. Tech.*, **7**, 3717–3735, doi.org/10.5194/amt-7-3717-2014, 2014.
- Mamouri, R. E. and Ansmann, A.: Estimated desert-dust ice nuclei profiles from polarization lidar: methodology and case studies, *Atmos. Chem. Phys.*, **15**, 3463–3477, doi.org/10.5194/acp-15-3463-2015, 2015.
- 495 Mamouri, R. E. and Ansmann, A.: Potential of polarization lidar to provide profiles of CCN- and INP-relevant aerosol parameters, *Atmos. Chem. Phys.*, **16**, 5905–5931, doi.org/10.5194/acp-16-5905-2016, 2016.
- Mamouri, R. E. and Ansmann, A.: Potential of polarization/Raman lidar to separate fine dust, coarse dust, maritime, and anthropogenic aerosol profiles, *Atmos. Meas. Tech.*, **10**, 3403–3427, doi.org/10.5194/amt-10-3403-2017, 2017.
- 500 Marinou, E., Tesche, M., Nenes, A., Ansmann, A., Schrod, J., Mamali, D., Tsekeri, A., Pikridas, M., Baars, H., Engelmann, R., Voudouri, K.-A., Solomos, S., Sciare, J., Groß, S., Ewald, F., and Amiridis, V.: Retrieval of ice-nucleating particle concentrations from lidar observations and comparison with UAV in situ measurements, *Atmos. Chem. Phys.*, **19**, 11315–11342, doi.org/10.5194/acp-19-11315-2019, 2019.
- Marcollì, C.: Deposition nucleation viewed as homogeneous or immersion freezing in pores and cavities, *Atmos. Chem. Phys.*, **14**, 2071–2104, doi.org/10.5194/acp-14-2071-2014, 2014.



- 505 Nakajima, T., Yoon, S. C., Ramanathan, V., Shi, G. Y., Takemura, T., Higurashi, A., Takamura, T., Aoki, K., Sohn, B. J., Kim, S. W., Tsuruta, H., Sugimoto, N., Shimizu, A., Tanimoto, H., Sawa, Y., Lin, N. H., Lee, C. T., Goto, D., and Schutgens, N.: Overview of the atmospheric brown cloud East Asian Regional Experiment 2005 and a study of the aerosol direct radiative forcing in east Asia, *J. Geophys. Res.*, 112, D24S91, doi.org/10.1029/2007JD009009, 2007.
- 510 Niemand, M., Möhler, O., Vogel, B., Vogel, H., Hoose, C., Connolly, P., Klein, H., Bingemer, H., DeMott, P., Skrotzki, J., and Leisner, T.: Parameterisation of immersion freezing on mineral dust particles: an application in a regional scale model, *J. Atmos. Sci.*, 69, 3077–3092, doi.org/10.1175/JAS-D-11-0249.1, 2012.
- Omar, A. H., Winker, D. M., Kittaka, C., Vaughan, M. A., Liu, Z., Hu, Y., Rogers, R. R., Ferrare, R. A., Lee, K.-P., Kuehn, R. E., and Hostetler, C. A.: The CALIPSO Automated Aerosol Classification and Lidar Ratio Selection Algorithm, *J. Atmos. Ocean Tech.*, 26(10), 1994-2014. doi.org/10.1175/2009JTECHA1231.1, 2009.
- 515 Peng, L., Yi, F., Liu, F., Yin, Z. and He, Y.: Optical properties of aerosol and cloud particles measured by a single-line-extracted pure rotational Raman lidar, *Opt. Express*, 29(14), 21947-21964. doi.org/10.1364/OE.427864, 2021.
- Prenni, A. J., DeMott, P. J., Rogers, D. C., Kreidenweis, S. M., McFarquhar, G. M., Zhang, G., and Poellot, M. R.: Ice nuclei characteristics from M-PACE and their relation to ice formation in clouds, *Tellus B*, 61, 436–448, doi.org/10.1111/j.1600-0889.2009.00415.x, 2009.
- 520 Righi, M., Hendricks, J., and Beer, C. G.: Exploring the uncertainties in the aviation soot–cirrus effect, *Atmos. Chem. Phys.*, 21, 17267–17289, doi.org/10.5194/acp-21-17267-2021, 2021.
- Spichtinger, P., and Cziczo, D.: Impact of heterogeneous ice nuclei on homogeneous freezing events in cirrus clouds, *J. Geophys. Res.*, 115, D14208, doi:10.1029/2009JD012168, 2010.
- Sporre, M. K., Friberg, J., Svenhag, C., Sourdeval, O., and Storelvmo, T.: Springtime stratospheric volcanic aerosol impact on midlatitude cirrus clouds, *Geophys. Res. Lett.*, 49, e2021GL096171, doi.org/10.1029/2021GL096171, 2022
- 525 Sourdeval, O., Gryspeerdt, E., Krämer, M., Goren, T., Delanoë, J., Afchine, A., Hemmer, F., and Quaas, J.: Ice crystal number concentration estimates from lidar-radar satellite remote sensing. Part 1: Method and evaluation, *Atmos. Chem. Phys.*, doi.org/10.5194/acp-2018-20, 2018.
- Steinke, I., Hoose, C., Möhler, O., Connolly, P., and Leisner, T.: A new temperature- and humidity-dependent surface site density approach for deposition ice nucleation, *Atmos. Chem. Phys.*, 15, 3703–3717, doi.org/10.5194/acp-15-3703-2015, 2015.
- 530 Tesche, M., Ansmann, A., Müller, D., Althausen, D., Engelmann, R., Freudenthaler, V., and Groß, S.: Vertically resolved separation of dust and smoke over Cape Verde using multiwavelength Raman and polarization lidars during Saharan Mineral Dust Experiment 2008, *J. Geophys. Res.*, 114, D13202. doi.org/10.1029/2009JD011862, 2009.
- 535 Tesche, M., Achtert, P., Glantz, P., and Noone, K. J.: Aviation effects on already-existing cirrus clouds, *Nat. Commun.*, 7, 12016, doi.org/10.1038/ncomms12016, 2016.

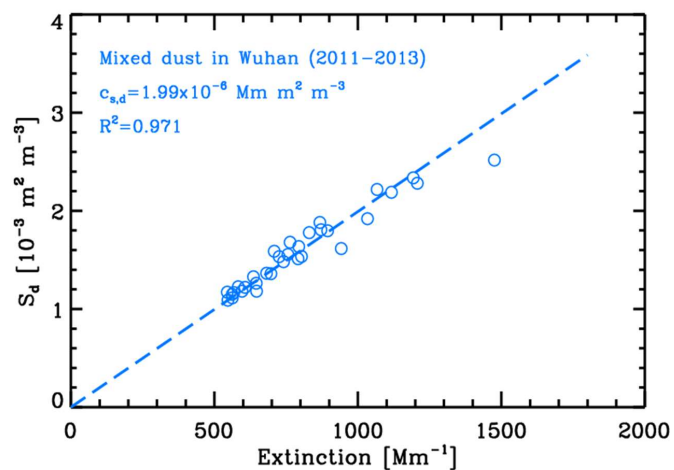


- Ullrich, R., Hoose, C., Möhler, O., Niemand, M., Wagner, R., Höhler, K., Hiranuma, N., Saathoff, H., and Leisner, T.: A new ice nucleation active site parameterization for desert dust and soot, *J. Atmos. Sci.*, 74, 699-717. doi.org/10.1175/JASD-16-0074.1, 2017.
- 540 Wang, W., Yi, F., Liu, F., Zhang, Y., Yu, C., and Yin, Z.: Characteristics and seasonal variations of cirrus clouds from polarization lidar observations at a 30°N plain site, *Remote Sens.*, 12, 3998, doi.org/10.3390/rs12233998020, 2020.
- Winker, D., Hunt, W., and McGill, M.: Initial performance assessment of CALIOP, *Geophys. Res. Lett.*, 34(19), L19803. doi.org/10.1029/2007GL030135, 2007.
- Wolf, V., Kuhn, T., and Krämer, M.: On the dependence of cirrus parametrizations on the cloud origin, *Geophys. Res. Lett.*, 46, doi.org/10.1029/2019GL083841, 2019.
- 545 Yang, K., Wang Z., Luo, T., Liu, X., and Wu, M.: Upper troposphere dust belt formation processes vary seasonally and spatially in the Northern Hemisphere, *Communications Earth & Environment*, 3(24), doi.org/10.1038/s43247-022-00353-5, 2022
- Yin, Z., Yi, F., He, Y., Liu, D., Yu, C., and Zhang, Y.: Asian dust impacts on heterogeneous ice formation at Wuhan based on polarization lidar measurements, *Atmos. Environ.*, 246(11), 118166, doi.org/10.1016/j.atmosenv.2020.118166, 2021.
- 550 Zhao, B., Wang, Y., Gu, Y., Liou K.-N., Jiang, J. H., Fan, J., Liu, X., Huang, L., and Yung, Y. L.: Ice nucleation by aerosols from anthropogenic pollution, *Nat. Geosci.*, 12, 602-607, doi.org/10.1038/s41561-019-0389-4, 2019.
- Zhao, X., Zhao, C., Yang, Y., Sun, Y., Xia, Y., Yang, X., and Fan, T.: Distinct changes of cloud microphysical properties and height development by dust aerosols from a case study over Inner-Mongolia region, *Atmos. Res.*, 273, 106175, doi.org/10.1016/j.atmosres.2022.106175, 2022.
- 555 Zhu, Q., Liu, Y., Shao, T., Luo, R., and Tan, Z.: A simulation study on the new transport pathways of global tropopause dust layer, *Geophys. Res. Lett.*, 48, e2021GL096063, doi.org/10.1029/2021GL096063, 2022.

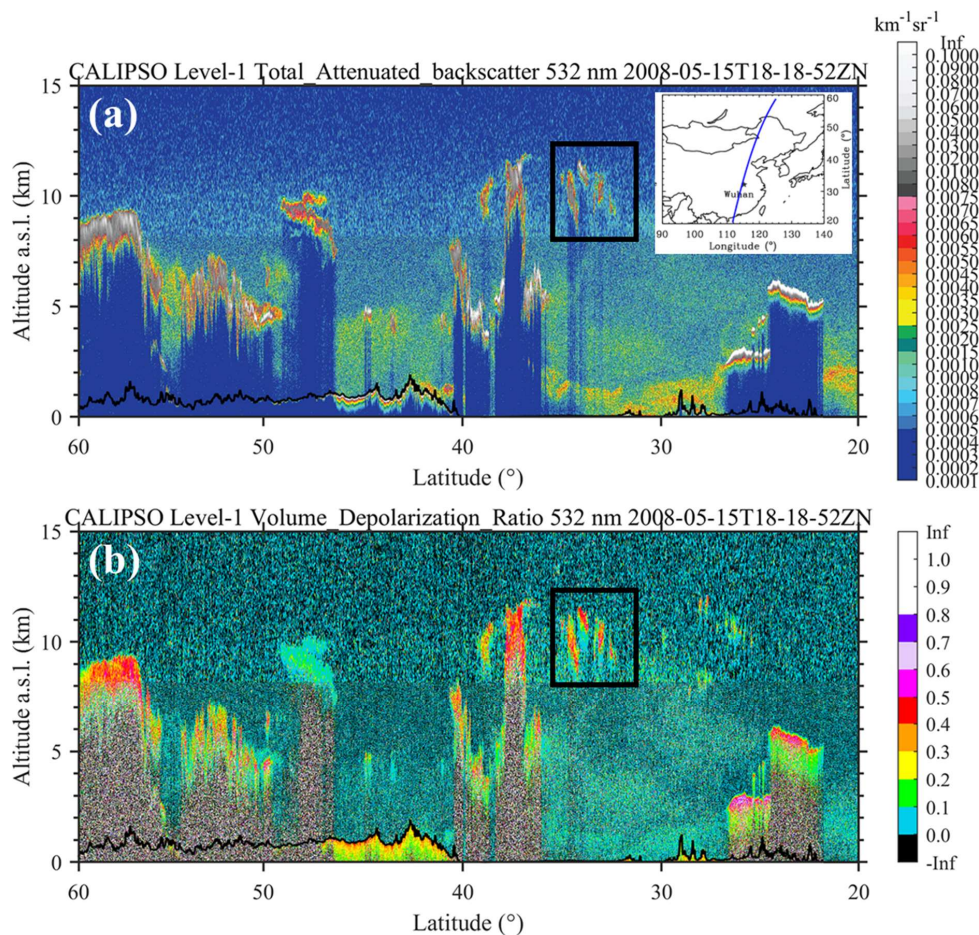


Table 1. Calculations for dust-related optical and ice-nucleating parameters (Tesche et al., 2009; Marinou et al., 2019; DeMott et al., 2010, 2015; Steinke et al., 2015; Ullrich et al., 2017). The estimated uncertainties in these parameters are also given (Ansmann et al., 2019b). The applicative temperature ranges are -30 to -14 °C for U17-I(d), -67 to -33 °C for U17-D(d) (Ullrich et al., 2017), -35 to -21 °C for D15 (DeMott et al., 2015), and -35 to -9 °C for D10 (DeMott et al., 2010), respectively. The profiles of temperature $T(z)$ (in Kelvin) and pressure $p(z)$ are provided by the most recently launched radiosonde in Wuhan; p_0 and T_0 are the standard pressure and temperature (Mamouri and Ansmann, 2015). n_s denotes the ice nucleation active site (INAS) density needed in the U17 parameterization scheme (Ullrich et al., 2017).

Dust-related parameters	Computation	Uncertainty	References
Dust backscatter β_d ($\text{Mm}^{-1} \text{sr}^{-1}$)	$\beta_d(z) = \beta_p(z) \frac{(\delta_p(z) - \delta_{nd})(1 + \delta_d)}{(\delta_d - \delta_{nd})(1 + \delta_p(z))}$ $\delta_d = 0.31, \delta_{nd} = 0.05$	10-30%	(Tesche et al., 2009)
Dust extinction α_d (Mm^{-1})	$\alpha_d(z) = LR_d \times \beta_d(z)$	15-25%	(Ansmann et al., 2019b)
Dust mass conc. M_d ($\mu\text{g m}^{-3}$)	$M_d(z) = \rho_d \times \alpha_d(z) \times c_{v,d}$ $\rho_d = 2.6 \text{ g cm}^{-3}$	20-30%	(Ansmann et al., 2019b)
Particle number conc. ($r > 250$ nm) $n_{250,d}$ (cm^{-3})	$n_{250,d}(z) = \alpha_d(z) \times c_{250,d}$	25-35%	(Ansmann et al., 2019b)
Particle surface conc. ($r > 100$ nm) $S_{100,d}$ ($\text{m}^2 \text{cm}^{-3}$)	$S_{100,d}(z) = \alpha_d(z) \times c_{s,d}$	30-40%	(Ansmann et al., 2019b)
D10 INP conc. n_{INP} (L^{-1})	$n_{\text{INP}}(p_0, T_0, T(z)) = a \cdot (273.16 - T(z))^b \cdot n_{250,d}(p_0, T_0)^{[c(273.16 - T(z)) + d]}$ $n_{\text{INP}}(z) = n_{\text{INP}}(p_0, T_0, T(z)) \cdot (T_0 p(z)) / (p_0 T(z))$ $\alpha = 0.0000594; b = 3.33; c = 0.0265; d = 0.0033$	50-500%	(DeMott et al., 2010)
D15 INP conc. n_{INP} (L^{-1})	$n_{\text{INP}}(p_0, T_0, T(z)) = f_d \cdot n_{250,d}(p_0, T_0)^{[a_d(273.16 - T(z)) + b_d]} \cdot \exp[c_d(273.16 - T(z)) + d_d]$ $n_{\text{INP}}(z) = n_{\text{INP}}(p_0, T_0, T(z)) \cdot (T_0 p(z)) / (p_0 T(z))$ $\alpha_d = 0; b_d = 1.25; c_d = 0.46; d_d = -11.6; f_d = 3.0$	50-500%	(DeMott et al., 2015)
U17-I(d) INP conc. n_{INP} (L^{-1})	$n_{\text{INP}}(z) = S_d(z) \times n_s(T(z))$ $n_s(T(z)) = \exp[150.577 - 0.517 \cdot T(z)]$	50-500%	(Ullrich et al., 2017)
U17-D(d) INP conc. n_{INP} (L^{-1})	$n_{\text{INP}}(z) = S_d(z) \times n_s(T(z), S_i)$ $n_s(T(z), S_i) = \exp\{\alpha_u(S_i - 1)^{1/4} \cos[b_u(T(z) - c_u)]^2 \cot^{-1}[d_u(T(z) - e_u)]/\pi\}$ $\alpha_u = 285.692; b_u = 0.017; c_u = 256.692; d_u = 0.08; e_u = 200.745$	50-500%	(Ullrich et al., 2017)
S15 INP conc. n_{INP} (L^{-1})	$n_{\text{INP}}(z) = S_d(z) \times n_s(T(z))$ $n_s(T(z)) = 1.88 \times 10^5 \cdot \exp[0.2659 \cdot \chi(T(z), S_i)]$ $\chi(T(z), S_i) = -(T(z) - 273.2) + (S_i - 1) \times 100$	50-500%	(Steinke et al., 2015)



570 **Figure 1.** Relationship between extinction coefficient and surface area concentration S_d for mixed dust in Wuhan. Correlations are given by sun photometer observations during dust-intrusion days that are verified by ground-based polarization lidar (He et al., 2021b). Each hollow circle denotes a pair of daily averaged values for the dust occurrence period of a dust-intrusion day. The slope of the dashed blue line is defined as the extinction-to-surface area conversion factor (Ansmann et al., 2019b). All the circles are obtained from the dust-intrusion days during 2011–2013.



575

Figure 2. CALIPSO altitude-orbit cross section measurements of the CALIOP Level-1B 532-nm (a) total attenuated backscatter coefficient and (b) volume depolarization ratio product on 15 May 2008. The corresponding orbit is 2008-05-15T18-18-56Z. The black rectangles mark the dust-related cirrus cloud.

580

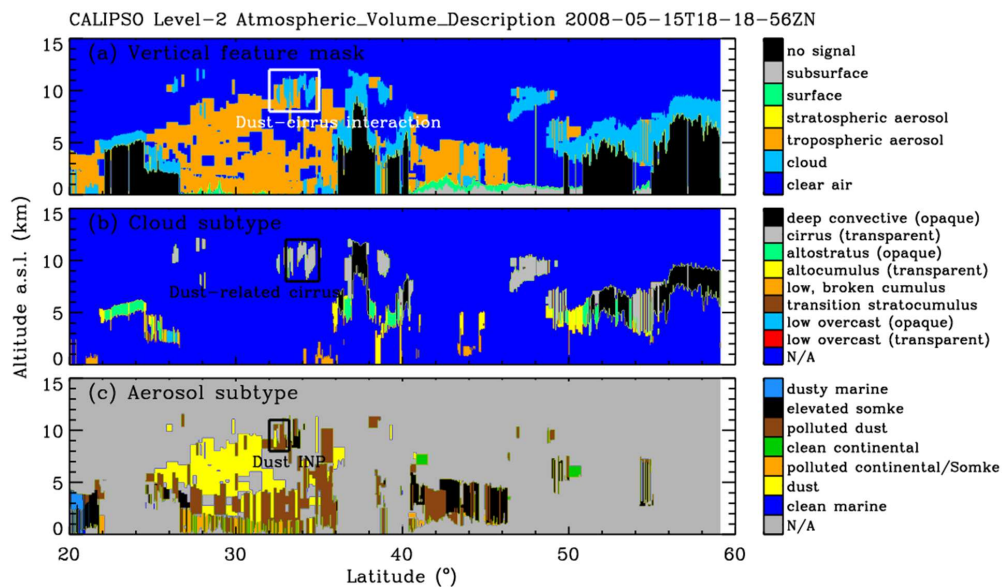


Figure 3. CALIPSO altitude-orbit cross section measurements of the CALIOP Level-2 (a) vertical feature mask, (b) cloud subtype, and (c) aerosol subtype product on 15 May 2008. The corresponding orbit is 2008-05-15T18-18-56Z. The footprint of the satellite is the same as shown in figure 2.

585

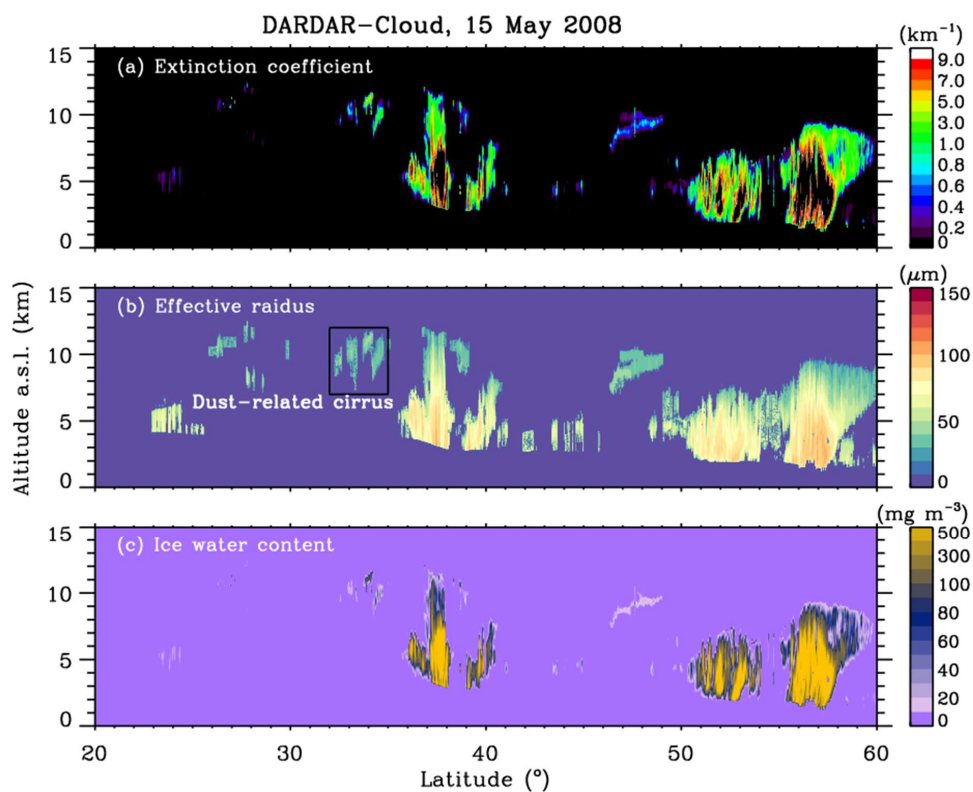
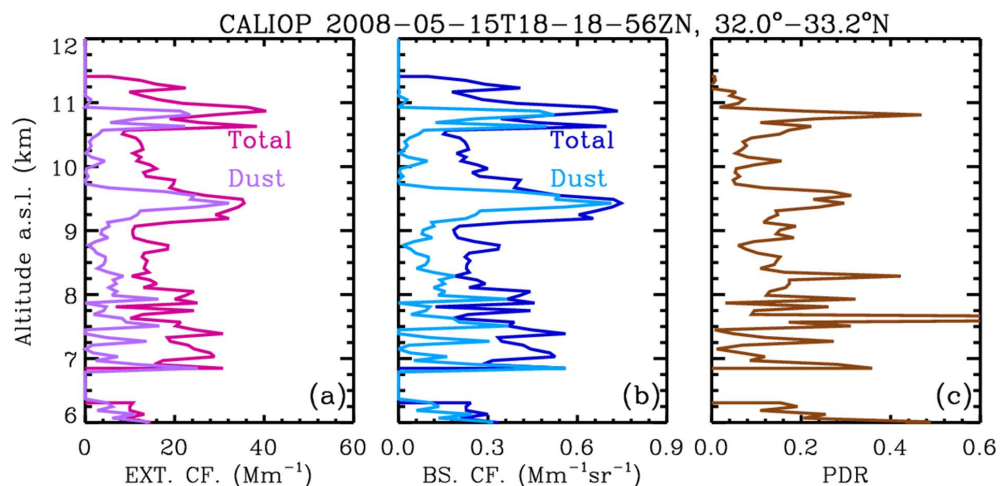
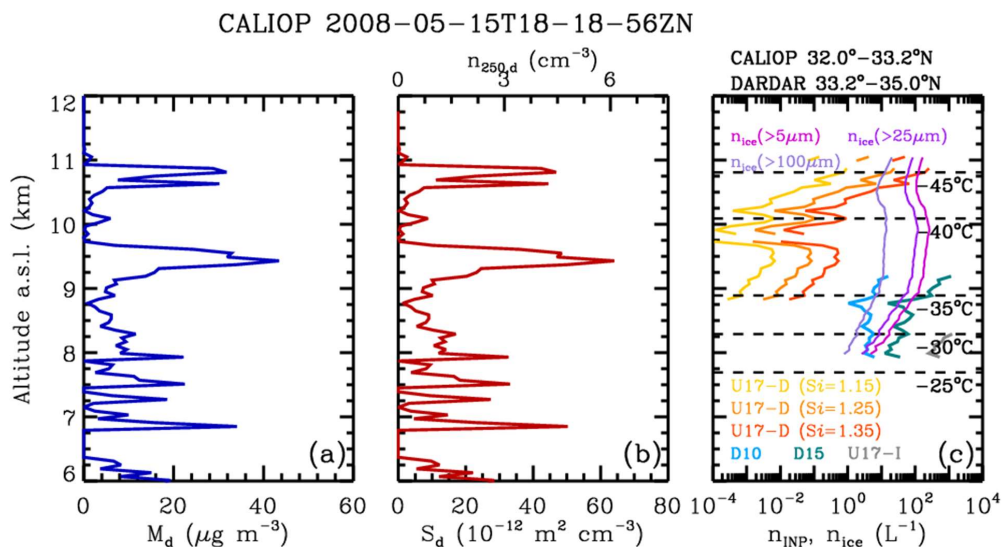


Figure 4. Altitude-orbit cross section of the (a) cloud extinction coefficient, (b) cloud particle effective radius, and (c) ice water content from the DARDAR-Cloud product on 15 May 2008. The footprint of the satellite is the same as shown in figure 2.



590

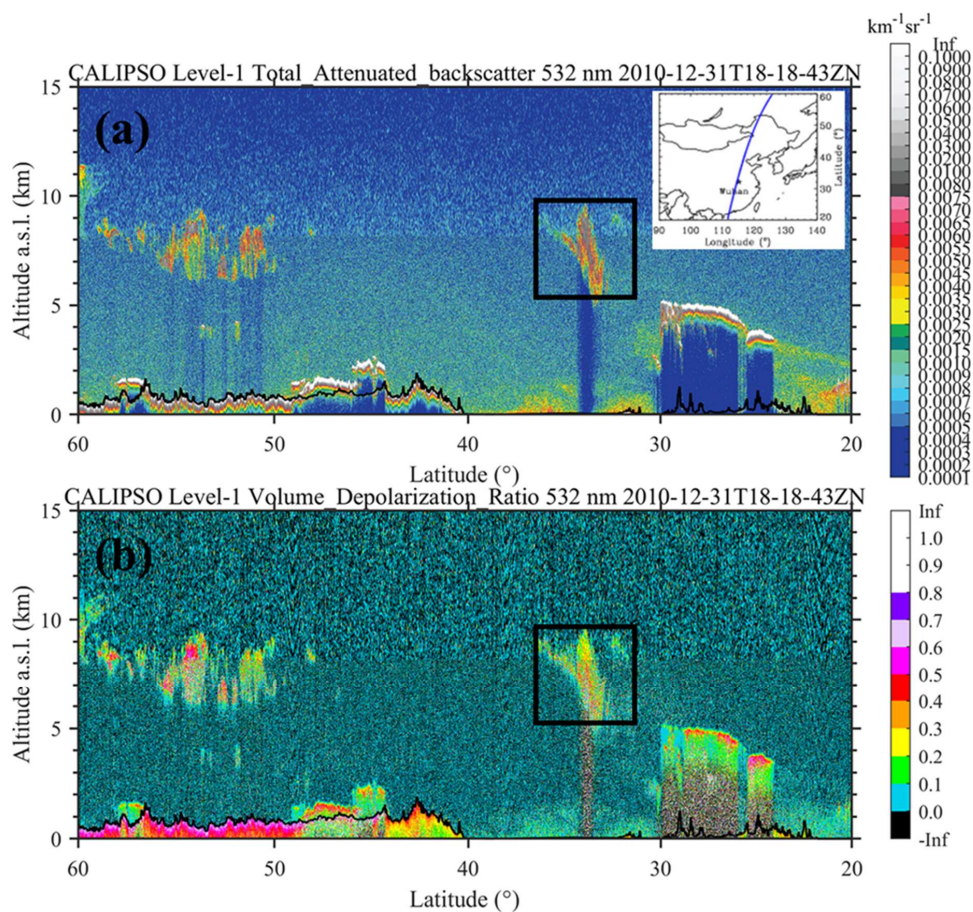
Figure 5. Profiles of the 532-nm (a) dust and total (dust + non-dust) extinction coefficient, (b) dust and total (dust + non-dust) backscatter coefficient, and (c) particle depolarization ratio obtained/calculated from the CALIOP Level-2 aerosol profile product on 15 May 2008. The profiles within the latitude range of 32.0-33.2°N are integrated here.



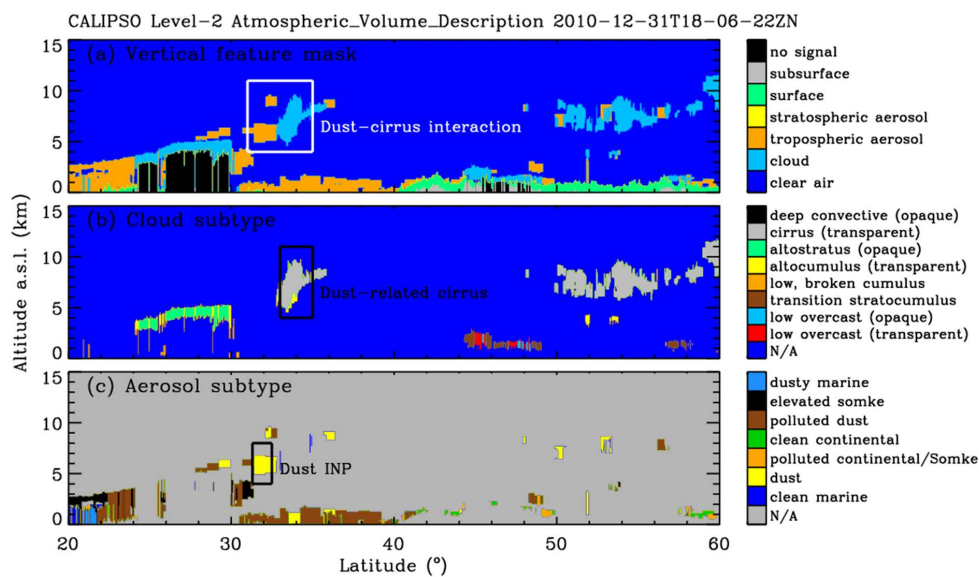
595

Figure 6. Profiles of the (a) dust mass concentration M_d , (b) particle number concentration (with radius >250 nm) $n_{250,d}$ and surface area concentration S_d , and (c) ice-nucleating particle concentration n_{INP} (derived by the POLIPHON method using the parameterization schemes of D10, D15, U17-D, and U17-I) and ice crystal number concentration n_{ice} (from DARDAR-Nice data product) on 15 May 2008. INP-related parameters are calculated from the dust-related optical properties given in figure 5 (corresponding to the CALIOP footprints between 32.0-33.2°N). For the DARDAR-Nice product, the profiles within the latitude range of 33.2-35.0°N are integrated.

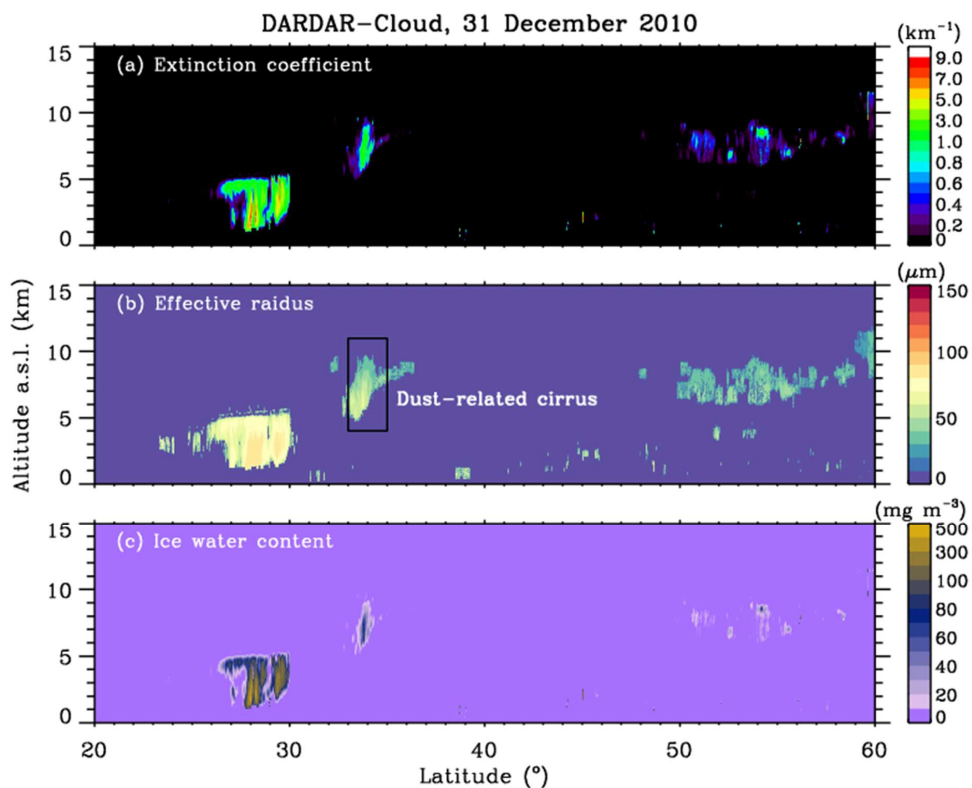
600



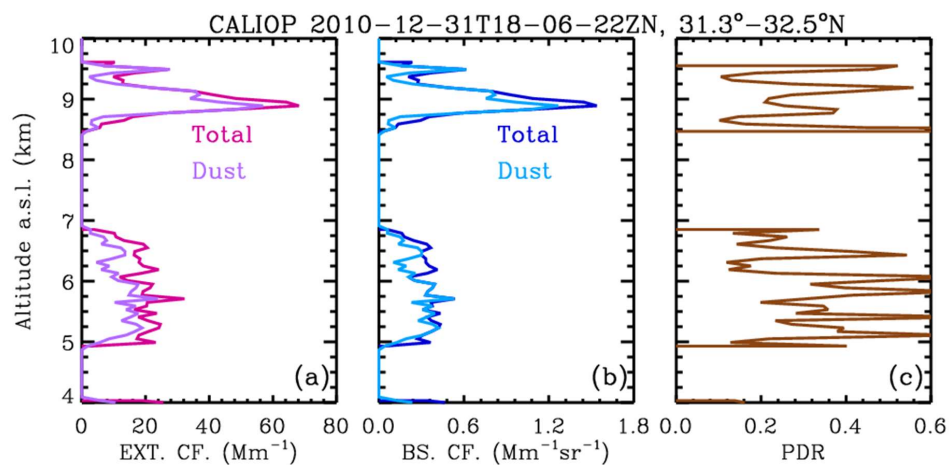
605 **Figure 7.** CALIPSO altitude-orbit cross section measurements of the CALIOP Level-1B 532-nm (a) total attenuated backscatter coefficient and (b) volume depolarization ratio product on 31 December 2010. The corresponding orbit is 2010-12-31T18-06-22Z. The black rectangles mark the dust-related cirrus cloud.



610 **Figure 8.** CALIPSO altitude-orbit cross section measurements of the CALIOP Level-2 (a) vertical feature mask, (b) cloud subtype, and (c) aerosol subtype product on 31 December 2010. The corresponding orbit is 2010-12-31T18-06-22Z. The footprint of the satellite is the same as shown in figure 7.



615 **Figure 9.** Altitude-orbit cross section of the (a) cloud extinction coefficient, (b) cloud particle effective radius, and (c) ice water content from the DARDAR-Cloud product on 31 December 2010. The footprint of the satellite is the same as shown in figure 7.



620 **Figure 10.** Profiles of the 532-nm (a) dust and total (dust + non-dust) extinction coefficient, (b) dust and total (dust + non-dust) backscatter coefficient, and (c) particle depolarization ratio obtained/calculated from the CALIOP Level-2 aerosol profile product on 31 December 2010. The profiles within the latitude range of 31.3-32.5°N are integrated here.

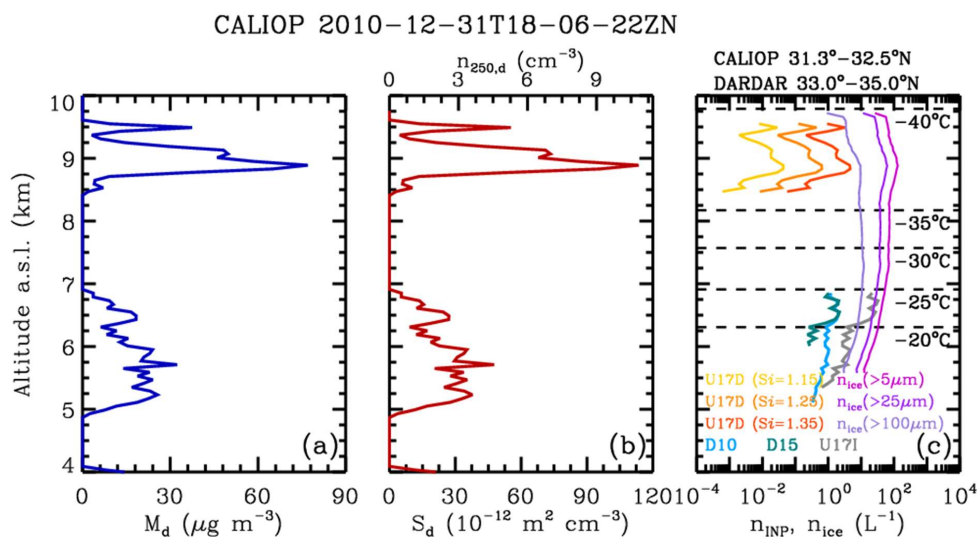


Figure 11. Profiles of the (a) dust mass concentration M_d , (b) particle number concentration (with radius >250 nm) $n_{250,d}$ and surface area concentration S_d , and (c) ice-nucleating particle concentration n_{INP} (derived by the POLIPHON method using the parameterization schemes of D10, D15, U17-D, and U17-I) and ice crystal number concentration n_{ice} (from DARDAR-Nice data product) on 31 December 2010. INP-related parameters are calculated from the dust-related optical properties given in figure 10 (corresponding to the CALIOP footprints between 31.3 - 32.5°N). For the DARDAR-Nice product, the profiles within the latitude range of 33.0 - 35.0°N are integrated.



630 **Table 2. Overview of in-cloud ICNC and dust INPC for the two cases on 15 May 2008 and 31 December 2010 in central China regions. The ICNC values are provided by the DARDAR Nice data product. The INPC values are retrieved from CALIOP dust extinction coefficient based on the POLIPHON method. The layer-averaging values for ICNC and INPC are given together with the minimum and maximum values in parentheses.**

Parameter	15 May 2008		31 December 2010
	Heterogeneous-sole nucleation	Competition between heterogeneous and homogeneous nucleation	Competition between heterogeneous and homogeneous nucleation
Altitude range of cirrus (km)	10.6 – 10.9 (upper part of the cirrus)	9.0 – 9.8 (lower part of the cirrus)	8.5 – 9.6 (upper part of the cirrus)
Latitude range of cirrus (°N)	32.0 – 33.2	32.0 – 33.2	33.0 – 35.0
Temperature range of cloud (°C)	-40 – -45	-35 – -40	-35 – -40
ICNC, $n_{ice,5\mu m}$ (L ⁻¹)	121.8 (108.3 – 140.4)	186.8 (129.8 – 233.1)	93.4 (59.8 – 129.7)
ICNC, $n_{ice,5\mu m}$ (L ⁻¹)	59.5 (51.1 – 70.6)	86.7 (60.8 – 106.8)	44.2 (27.5 – 62.1)
ICNC, $n_{ice,5\mu m}$ (L ⁻¹)	11.6 (8.2 – 15.8)	11.2 (8.5 – 12.4)	6.6 (3.4 – 9.6)
Altitude range of dust layer (km)	10.6 – 10.9	9.0 – 9.8	8.5 – 9.6
Latitude range of dust layer (°N)	33.2 – 35.0	33.2 – 35.0	31.3 – 32.5
Dust INP, U17-D, Si=1.15 (L ⁻¹)	0.405 (0.042 – 0.931)	0.003 (0 – 0.007)	0.016 (0.002 – 0.043)
Dust INP, U17-D, Si=1.25 (L ⁻¹)	9.897 (0.891 – 23.875)	0.041 (0.001 – 0.083)	0.232 (0.028 – 0.641)
Dust INP, U17-D, Si=1.35 (L ⁻¹)	102.792 (8.341 – 256.571)	0.259 (0.010 – 0.527)	1.667 (0.202 – 4.672)

635

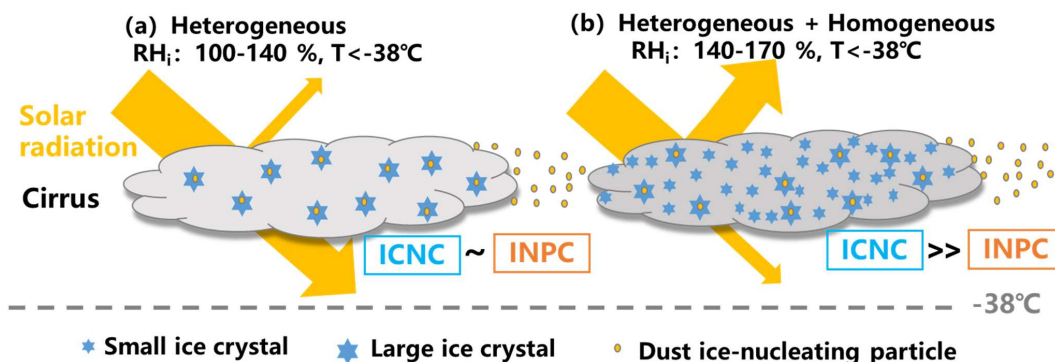


Figure 12. Schematic illustration of the two ice-nucleating mechanisms of the dust-related cirrus clouds (i.e., cirrus occurs accompanied by dust particles ambient). (a) Heterogeneous nucleation solely takes place with the RH_i of 100-140% and temperature of < 0°C. The ice crystals within the cirrus are relatively larger and the ICNC within the cirrus is comparable to the ambient dust INPC. This type of cirrus is always more transparent and allows more solar radiation to enter the middle and lower troposphere. (b) Competition between heterogeneous and homogeneous nucleation with the RH_i of 140-170% and temperature of < -38°C. Besides the large ice crystals formed by heterogeneous nucleation, there are also numerous smaller ice crystals within the cirrus produced via homogeneous nucleation (Krämer et al., 2020). The ICNC within the cirrus is far beyond (one to several orders of magnitude) the ambient dust INPC (Froyd et al., 2022). This type of cirrus is optically denser and can reflect more solar radiation into space, resulting in the partial offset of the total net warming effect of cirrus clouds on the Earth's atmosphere (Kuebbeler et al., 2014; Lohmann and Gasparini, 2017).